AGU ADVANCING EARTH AND SPACE SCIENCES

JGR Atmospheres

RESEARCH ARTICLE
10.1029/2025JD045114

Mechanisms Controlling Dust Aerosol Collection by Isolated Obstacles Near the Ground

Kang Gong[1,2], Jie Zhang[3,4], Qi Chen[5], Xiangyu Xi[5], Xuan Cheng[5], Ning Huang[3,4], and Zhongwei Huang[1,2]

[1]Key Laboratory for Semi-Arid Climate Change of the Ministry of Education, College of Atmospheric Sciences, LanzhouUniversity, Lanzhou, China, [2]Collaborative Innovation Center for Western Ecological Safety, Lanzhou University, Lanzhou, China, [3]Key Laboratory of Mechanics on Disaster and Environment in Western China, Lanzhou University, the Ministry of Education of China, Lanzhou, China, [4]Department of Mechanics, School of Civil Engineering and Mechanics, Lanzhou University, Lanzhou, China, [5]Deep Space Exploration Laboratory, Beijing, China

Key Points:

- Turbulence around near-ground obstacles significantly affects the deposition of airborne dust aerosol particles
- Particle size, wind speed, and obstacle dimensions jointly influence particle collection efficiency
- The improved model predicts particle deposition on near-ground obstacle surfaces with higher accuracy

Correspondence to:

N. Huang and Z. Huang,
huangn@lzu.edu.cn;
huangzhongwei@lzu.edu.cn

Citation:

Gong, K., Zhang, J., Chen, Q., Xi, X., Cheng, X., Huang, N., & Huang, Z. (2026). Mechanisms controlling dust aerosol collection by isolated obstacles near the ground. *Journal of Geophysical Research: Atmospheres*, *131*, e2025JD045114. https://doi.org/10.1029/2025JD045114

Received 8 AUG 2025
Accepted 12 JAN 2026

Author Contributions:

Conceptualization: Kang Gong, Jie Zhang, Ning Huang, Zhongwei Huang
Data curation: Kang Gong, Jie Zhang, Qi Chen, Xiangyu Xi, Xuan Cheng, Ning Huang, Zhongwei Huang
Formal analysis: Kang Gong, Jie Zhang, Qi Chen, Xiangyu Xi, Xuan Cheng, Ning Huang, Zhongwei Huang
Funding acquisition: Jie Zhang, Ning Huang
Investigation: Kang Gong, Qi Chen, Xiangyu Xi, Xuan Cheng, Ning Huang, Zhongwei Huang
Methodology: Kang Gong, Jie Zhang, Ning Huang, Zhongwei Huang
Project administration: Jie Zhang, Ning Huang
Resources: Kang Gong, Jie Zhang, Qi Chen, Xiangyu Xi, Xuan Cheng, Ning Huang, Zhongwei Huang
Software: Kang Gong, Qi Chen, Xiangyu Xi, Xuan Cheng
Supervision: Jie Zhang, Qi Chen, Xiangyu Xi, Xuan Cheng, Ning Huang, Zhongwei Huang
Validation: Kang Gong
Visualization: Kang Gong, Jie Zhang
Writing – original draft: Kang Gong

Abstract The collection of dust aerosols (0.1–10 μm) by near-surface obstacles is one of the important processes in atmospheric aerosol dry deposition. However, existing understanding of this process remains limited. For example, most current deposition models assume complete deposition or describe the collection process through empirical models, making it difficult to accurately predict the concentration distribution of dust particles within the near-surface collection layer. In this study, the effects of turbulence around obstacles are considered to improve an existing numerical model for simulating aerosol particle deposition in rough surface environments. The modified numerical model is validated through wind tunnel experiments. Subsequently, the particle collection process on an isolated cylindrical obstacle placed on the ground is investigated using numerical simulations. The effects of different wind conditions, particle properties, and obstacle sizes on the collection process are analyzed. Finally, a fitted relationship between the Stokes number and collection efficiency is proposed. The results show that inertial impaction and interception jointly dominate particle deposition on the windward side of the isolated obstacle, while turbulence-induced impaction governs deposition on the leeward side. Therefore, parameters that affect particle inertia and the turbulent flow around the obstacle have a more significant impact on the particle deposition process. The simulation results agree well with existing experimental data and exhibit lower data dispersion, demonstrating that the numerical model developed in this study can effectively describe the collection of particles by near-surface obstacles. This provides a solid basis for improving atmospheric particle deposition models.

Plain Language Summary When dust aerosols (0.1–10 μm) approach the ground, they can be retained by various ground objects. This process is of pivotal importance in the removal of dust aerosols from the atmosphere. However, the scientific community's understanding of the interactions between these particles and ground surfaces remains limited. Consequently, it is challenging to predict the concentration distribution of particles that will settle in close proximity to the ground. To address this issue, this study improved a numerical model to simulate the process of particle deposition on the surface of a single cylindrical object placed on the ground. Our research results indicate that the ease of particle deposition is closely related to the particles' capacity to resist changes in motion (inertia) and the flow characteristics of the air around the object. The model shows high consistency with experimental data from other studies and provides higher data quality. This makes it a useful tool for improving predictions of how particles settle near the ground, which can support environmental research and air quality modeling.

1. Introduction

The circulation of dust aerosols in the atmosphere primarily involves three sequential processes: entrainment, transport, and deposition, which collectively facilitate material exchange across different regions (Mahowald et al., 2005; Pye, 2015; Shao et al., 2011). In dust source regions, particles on the ground surface obtain kinetic energy from the airflow and are entrained by fluid dynamics. Larger particles quickly fall back to the ground and collide with particles on the ground surface, causing more particles to be emitted into the air through impact. Meanwhile, finer particles may be lofted into the upper atmosphere by turbulence, allowing for long-range and long-duration transport. In regions with weaker turbulence, these fine particles gradually settle out of the atmosphere under the combined influence of gravity, turbulence, and precipitation, ultimately depositing onto near-

Writing – review & editing: Kang Gong, Jie Zhang, Ning Huang, Zhongwei Huang

surface obstacles (Pye, 2015). Simultaneously, harmful substances adsorbed onto the surfaces of dust particles are co-deposited in the receiving regions, potentially affecting human health and environmental quality (Martinelli et al., 2013).

Dry deposition, as the dominant particle deposition mechanism under non-precipitating weather conditions and in arid and semi-arid regions (Pan & Wang, 2015), exhibits broad spatial and temporal distribution across the atmospheric boundary layer and serves as the primary pathway for the removal of most atmospheric particulates. Therefore, this study focuses on the dry deposition of atmospheric particles. Shao (2008) categorized dry deposition into two distinct regimes: in regions away from the ground surface, particle deposition is primarily governed by atmospheric turbulence and gravitational forces; In the near-surface region, particles are collected by obstacles under the combined influence of various mechanisms, which is also the final step in the particle dry deposition process. In conventional atmospheric models, the particle concentration within the collection layer (C_0) is often assumed to be zero, implying complete and irreversible deposition within this region. Although this assumption simplifies the implementation of deposition models, it limits accuracy; thus, further investigation into particle deposition within the near-surface layer is necessary to improve the accuracy of model predictions.

In most studies, near-surface obstacles are commonly idealized as cylindrical structures (Malet et al., 2000; Smoke, 1977; Zhang & Shao, 2014), and previous research has identified four primary mechanisms governing particle deposition on cylindrical surfaces: inertial impaction, interception, Brownian diffusion, and rebound (Petroff et al., 2008a). Among these, inertial impaction involves the deposition of large particles on the windward side of the obstacle due to inertial forces, while smaller particles may deposit on the leeward side via turbulence-induced impaction (Petroff et al., 2008b). Interception refers to the process by which some well-followed but large-sized particles, when following the fluid around an obstacle, are captured due to their large size hitting the surface of the obstacle (Droppo, 2006; Fuchs et al., 1965). Brownian diffusion describes the random motion of particles that causes them to deviate from fluid streamlines and collide with the obstacle surface (Droppo, 2006). Rebound refers to the phenomenon wherein particles, upon colliding with the obstacle, fail to adhere to the surface and instead bounce off, thereby reducing overall collection efficiency (Chamberlain, 1968). Among all mechanisms, inertial impaction is generally the dominant contributor to particle deposition. However, the relative contribution of each mechanism varies with changes in obstacle geometry, particle properties and flow field characteristics.

To quantitatively describe the particle collection process on obstacle surfaces, Bache (1979) defining the collection efficiency as the ratio of the deposition flux on the obstacle surface to the incoming particle flux across the obstacle's frontal area. Based on this definition, the particle collection efficiency for a single obstacle can be calculated using the following equation:

$$E = \frac{\text{Trap dose}}{\text{Area dose}} = \frac{M}{CUd_c h_c t}, \tag{1}$$

here, M denotes the total mass of particles deposited on the obstacle surface during a time period t, C is the time-averaged particle concentration in front of the obstacle, U is the local time-averaged wind speed at the obstacle center height, d_c and h_c are the characteristic width and height of the obstacle, respectively.

Several researchers have investigated the particle collection process by near-surface obstacles using various approaches based on the definition of collection efficiency. Marple and Liu (1974) developed a theoretical model to analyze particle impact positions on various impaction surfaces and provided analytical expressions for collection efficiency under laminar flow conditions. By integrating drag-partition theory with particle-collection mechanisms, Zhang and Shao (2014) proposed a new deposition scheme that achieves markedly improved agreement with wind-tunnel measurements. Moran et al. (2013) conducted wind tunnel experiments to examine particle collection on thin plate surfaces, focusing on the influence of isotropic turbulence on surface deposition. They also modified the classical Stokes number to incorporate turbulent effects. To further investigate the impact of geometries on particle deposition, Price et al. (2017) extended Moran's work by using natural vegetation surfaces to study particle collection in the non-inertial collision regions on the leeward side of obstacles. They proposed an improved parameterization scheme for effective deposition area, resulting in lower dispersion of experimental results. However, these studies have certain limitations, particularly in their inability to quantify the spatial distribution of particle deposition on obstacle surfaces, which hinders further analysis of location-specific

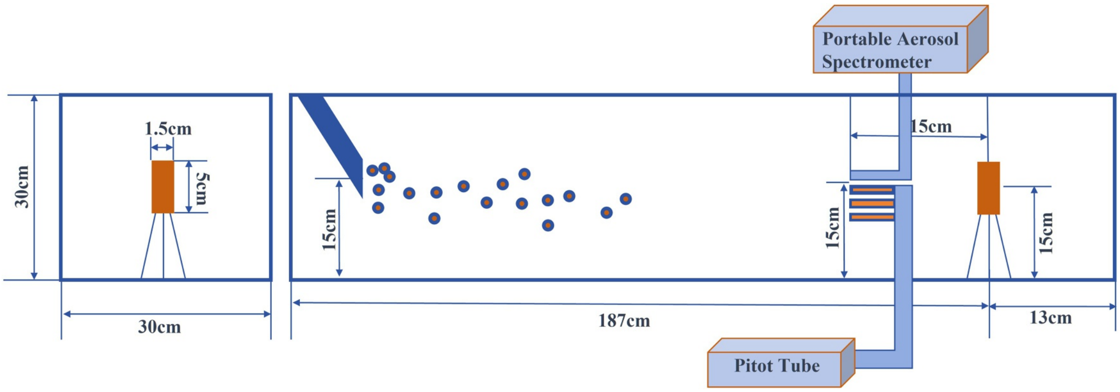

Figure 1. Schematic of the wind-tunnel experimental setup. The orange object is the obstacle (made of 3D-printed polylactic acid) and the circles denote the released particles. The figure only illustrates the relative positions of the devices; during the formal deposition runs these instruments are removed to avoid disturbing the flow field.

deposition mechanisms. As a modern research tool, numerical simulation enables comprehensive acquisition of flow field variables and allows for detailed analysis of particle-obstacle interactions at high spatial and temporal resolutions. Nevertheless, studies utilizing numerical approaches to examine the micro-scale mechanisms of particle deposition on obstacle surfaces remain scarce in the current literature.

This study investigates the particle collection process on the surface of an isolated cylindrical obstacle by integrating wind tunnel experiments with numerical simulations. A wind tunnel experiment of the particle deposition process on isolated surfaces was conducted to validate the modified numerical simulation program. Since experimental methods are limited in resolving the complete microphysical processes of particle deposition across different regions of the obstacle surface—processes that are critical for understanding the underlying mechanisms—numerical simulations were further employed to elucidate the dominant deposition mechanisms in various surface zones of the obstacle. Additionally, the simulations were used to analyze how flow velocity, particle properties, and obstacle size influence the deposition process. The findings provide a theoretical basis for refining the physical parameterizations of particle deposition module in atmospheric deposition models, thereby improving the accuracy of model predictions.

2. Wind Tunnel Arrangement and Experimental Procedures

The wind tunnel consists of three sections: the drive section, the flow conditioning section, and the test section. The layout of the test section is illustrated in Figure 1. The left panel shows the cross-sectional dimensions of both the wind tunnel and the cylindrical obstacle. The dimensions of the test section were 2.0 m in length, 0.3 m in width, and 0.3 m in height. A cylindrical obstacle with a diameter of 1.5 cm and a height of 5.0 cm was placed 1.87 m downstream from the inlet of the test section, centered along the vertical midline of the tunnel. The front view presents the relative positions of the experimental instruments. The cylindrical obstacle was produced using an Ender-3S 3D printer with a printing resolution of 0.1 mm. Because an excessively smooth surface may cause deposited particles to slide or be blown away, a layer of 120-grit sandpaper was attached to the cylinder surface to increase its roughness.

Prior to the formal initiation of the experiment, the flow fields generated by fans operating at different rotational speeds were measured. A Pitot tube was used to record wind velocities at various heights, positioned 15 cm upstream of the cylindrical obstacle. Subsequently, the concentration and particle size distribution of the generated aerosols were measured at the obstacle location using a Portable Aerosol Spectrometer. It is an optical instrument manufactured by Grimm (Germany), model Portable Laser Aerosol Spectrometer and Dust Monitor 1.109. This instrument is widely used in wind-tunnel and field measurements because of its simple operation, reliable data quality, compact design, and long battery life. The airflow velocity and aerosol concentration were measured over a 3 min period prior to each deposition experiment. After these 3-min measurements, both the Pitot tube and the aerosol spectrometer were removed from the wind tunnel to avoid disturbing the flow field. The aerosol solution used in the experiment followed a preparation method similar to that described by Moran et al. (2013). It consisted of a mixture of distilled water and glycerol at a volume ratio of 3.75:1, into which sodium

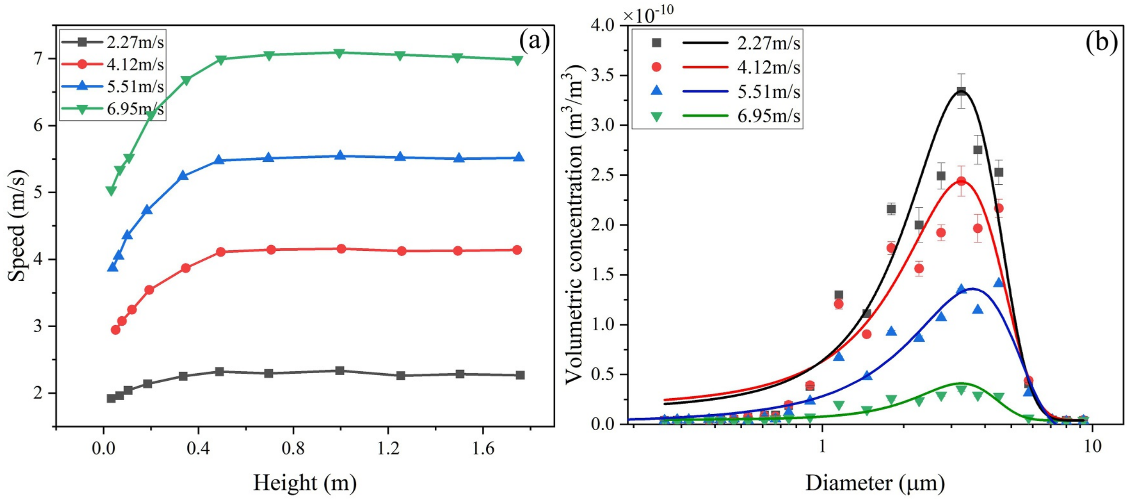

Figure 2. Wind speed and particle concentration data measured at different wind speeds in the wind tunnel experiment. (a) Wind speed profile 15 cm in front of the obstacle; (b) Average particle concentration at the location of the obstacle.

fluorescein ($C_{20}H_{10}Na_2O_5$) powder was dissolved. For each experimental run, 1L of the prepared solution was placed into an ultrasonic nebulizer. Aerosol particles were introduced into the wind tunnel via a PVC pipeline from the inlet of the test section. Before the experiments, we prepared a series of solutions with known concentrations of sodium fluorescein and measured their fluorescence intensity using a fluorescence spectrophotometer. This yielded a linear relationship between fluorescence intensity F_i and sodium fluorescein concentration C_{Na}: $F_i = 3.427 \times 10^7 \bullet C_{Na} - 13.118$. After each experiment, the cylindrical obstacle was rinsed three times with distilled water. The rinsing water was collected to obtain a solution containing the deposited sodium fluorescein, and its fluorescence intensity was measured with the same spectrophotometer. Using the above calibration relationship, we determined the concentration of sodium fluorescein in the rinsing solution and, from this, calculated the total mass of particles deposited on the obstacle surface. The total mass of particles deposited on the obstacle surface was then determined through weighted summation. The particle collection efficiency was calculated using Equation 1.

In the experiment, the wind speed profiles corresponding to different fan rotational speeds are shown in Figure 2a. It can be observed that, under all tested conditions, the airflow stabilized at a height of 15 cm—the centerline of the wind tunnel. Figure 2b presents the aerosol concentration distributions measured at the obstacle location under four different wind speeds, each corresponding to a distinct fan speed. Since the particle release rate remains constant across different wind speeds, the average particle concentration in the wind tunnel decreases as the wind speed increases. The particle size distribution followed a log-normal pattern, with peak concentrations occurring when the particle diameter (D_p) ranged between 2 μm and 4 μm. As the wind speed increased, the peak particle concentration gradually decreased. This trend was attributed to the enhancement of turbulent fluctuations at higher wind speeds, which intensified turbulent diffusion of the particles. Since the particle release rate remained constant across all conditions, the average particle concentration in the test section decreased with increasing wind speed. The volume-weighted average of the particle size data obtained from the spectrometer was used to determine the effective diameter of the aerosol particles in this experiment, which was calculated as 2.82 μm. Given the small initial size of the atomized droplets, rapid evaporation of water occurred after particle release. Therefore, the transported particles within the wind tunnel were considered to be composed of a glycerol–sodium fluorescein mixture, and the particle density was approximated using the density of glycerol, taken as 1,260 kg/m^3. To ensure sufficient particle deposition on the obstacle surface and to minimize experimental error, the duration of each experimental run was set to 20 min.

3. Basic Models and Control Equations for Numerical Simulation

Currently, there are four main numerical approaches for simulating two-phase flows (Gu, 2007): the Lagrangian particle-tracking model, the Euler-Euler two-fluid model, the homogeneous flow model, and the Euler-Lagrange segregated flow model. Among these, the Lagrangian particle-tracking model treats the particle phase as a discrete set of entities and applies Newton's second law to track the motion of each individual particle. The particle velocity is coupled with the continuous fluid phase to determine the instantaneous spatial distribution of particles. In contrast, the other three models treat the particle phase as a continuous medium, sacrificing particle-level resolution for computational efficiency. These continuum-based models are more appropriate for simulating highly flow-following particles. Given that this study involves particles with varying degrees of flow-following behavior in the atmosphere and aims to capture their deposition processes on obstacle surfaces, the Lagrangian particle-tracking model was selected. This approach enables accurate characterization of particle motion and their interactions with obstacles surface.

3.1. Flow Field Control Equations

In this study, the incompressible Navier-Stokes equations were used to describe the fluid phase, incorporating the feedback force exerted by particles on the flow field (Ma & Zheng, 2011; Tong & Huang, 2012). The governing equations are expressed as follows:

$$\begin{aligned} &\frac{\partial \overline{u_i}}{\partial x_i} = 0, \\ &\frac{\partial \overline{u_i}}{\partial t} + \frac{\partial \overline{u_i u_j}}{\partial x_j} = F_i - \frac{1}{\rho}\frac{\partial \overline{p}}{\partial x_i} + \frac{\partial}{\partial x_j}\left((\nu + \nu_t)\frac{\partial \overline{u_i}}{\partial x_j}\right), \end{aligned} \tag{2}$$

here, $\overline{u_i}$ and x_i represent the resolved velocity component and position in the i-th direction, respectively, where $i = 1,2,3$ corresponds to the streamwise (x), spanwise (y), and vertical (z) directions of the flow field. The variable t denotes time. The terms ρ, p, ν, and ν_t represent fluid density, pressure, kinematic viscosity, and eddy viscosity, respectively. The term F_i denotes the feedback force exerted by particles on the flow field in the i-th direction.

$$F_i = \frac{1}{V_{\text{cell}}}\sum_{n=1}^{n_{p\text{cell}}}\frac{1}{2}C_{dp}A_p|\overline{u} - u_p|\,(\overline{u_i} - u_{pi}), \tag{3}$$

in the equations, V_{cell} denotes the volume of a computational grid cell, and $n_{p\text{cell}}$ represents the number of particles within that cell. A_p is the cross-sectional area of a particle. $\overline{u}$ and u_p are the local fluid velocity and the particle velocity, respectively. C_{dp} denotes the drag coefficient of the particle.

This study primarily focused on simulating fine particles with diameters smaller than 10 μm. Assuming the particles to be spherical, the drag coefficient C_{dp} can be expressed as follows (Clift et al., 1978):

$$C_{dp} = \begin{cases} \dfrac{24}{Re_p} + \dfrac{6}{1+\sqrt{Re_p}} + 0.4, & Re_p \le 1000 \\ 0.424. & Re_p > 1000 \end{cases} \tag{4}$$

Re_p denotes the particle Reynolds number:

$$Re_p = \frac{|\overline{u} - u_p|\,D_p}{\nu}, \tag{5}$$

D_p represents the particle diameter.

In this study, the Improved Delayed Detached Eddy Simulation (IDDES) model was selected as the turbulence model. The IDDES approach is an extension of the $k-\omega$ Shear Stress Transport (SST) model. The $k-\omega$ turbulence model is a commonly used two-equation closure for the Reynolds-averaged Navier-Stokes (RANS) equations. It solves transport equations for the turbulent kinetic energy k and the specific dissipation rate ω, where k quantifies the intensity of turbulence and ω characterizes the rate at which this energy is dissipated into internal thermal energy. Menter (1994) incorporated the effects of shear-stress transport into the formulation of turbulent

10.1029/2025JD045114

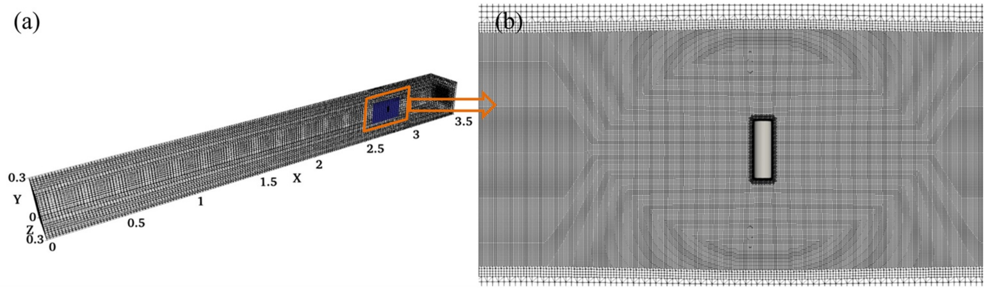

Figure 3. Schematic of the computational domain (a) and local refinement of grid (b).

viscosity, leading to the development of the $k - \omega$ SST model, which provides improved performance in adverse pressure-gradient and separated flows. For incompressible flows, the governing equations for k and ω are:

$$\begin{aligned} &\frac{\partial k}{\partial t} + u_j \frac{\partial k}{\partial x_j} = \tau_{ij} \frac{\partial u_i}{\partial x_j} - \beta^* k\omega + \frac{\partial}{\partial x_j}\left((\nu + \sigma_k \nu_t) \frac{\partial k}{\partial x_j} \right), \\ &\frac{\partial \omega}{\partial t} + u_j \frac{\partial \omega}{\partial x_j} = \frac{\gamma_2}{\nu_t} \tau_{ij} \frac{\partial u_i}{\partial x_j} - \beta\omega^2 + \frac{\partial}{\partial x_j}\left((\nu + \sigma_\omega \nu_t) \frac{\partial \omega}{\partial x_j} \right) + 2(1 - F_1)\sigma_{\omega 2} \frac{1}{\omega} \frac{\partial k}{\partial x_j} \frac{\partial \omega}{\partial x_j}, \end{aligned} \tag{6}$$

where kinematic eddy viscosity $\nu_t = a_1 k / \max(a_1 \omega, SF_2)$, S is the magnitude of the vorticity. Closure coefficients F_1 and F_2 are defined in Menter (1994), All remaining model constants and auxiliary relations (e.g., $CD_{k\omega}$) follow the standard $k - \omega$ SST formulation. The main advantage of IDDES lies in its hybrid formulation: in near-wall regions where the grid resolution is insufficient for Large Eddy Simulation (LES), the model reverts to RANS modeling to ensure adequate accuracy while minimizing computational cost. Away from the wall, LES is employed to resolve large-scale turbulent structures. The IDDES model has been successfully applied in numerous studies involving complex wall-bounded flows, yielding reliable results (Gong et al., 2024; Saini et al., 2018; Xu et al., 2018). More detailed descriptions of the model can be found in Gritskevich et al. (2012).

3.2. Particle Equations of Motion

The motion of dust aerosol particles was described by Newton's second law:

$$m_p \frac{du_{pi}}{dt} = \frac{1}{6}\pi(\rho_p - \rho) D_p^3 g + \frac{1}{2} C_{dp} A_p |\overline{u} - u_p| (\overline{u_i} - u_{pi}) + G\sqrt{\frac{2K^2T^2}{D\Delta t}}, \tag{7}$$

on the right-hand side of the equation, the first term represents the effect of gravity and buoyancy. The second term corresponds to the drag force F_D, where ρ_p and g denote the particle density and gravitational acceleration, respectively. The third term accounts for the fluctuating force arising from the turbulent flow field on the particles (Li & Ahmadi, 1992), which is related to the turbulent kinetic energy (K), flow temperature (T), and particle diffusivity (D). The particle diffusivity is given by $D = \frac{kT}{\beta m}$, where k is the Boltzmann constant and $\beta = \frac{3\pi\mu d}{C_c m}$. The Cunningham correction factor is defined as $C_c = 1 + \frac{2\lambda_m}{D_p}\left(1.257 + 0.4e^{\frac{0.55D_p}{\lambda_m}}\right)$, where λ_m is the mean free path of air molecules, defined as the average distance traveled by a particle between two successive collisions (Chapman & Cowling, 1990), and is given by $\lambda_m = \frac{k_b T}{\sqrt{2}\pi D_p^2 \rho_p}$. The stochastic fluctuation component is represented by $G = \sqrt{-2 \ln U_1} \cos 2\pi U_2$, where U_1 and U_2 are independent random numbers uniformly distributed in the interval (0, 1). Other variables retain their definitions as introduced in Equations 2–5.

3.3. Parameter Setting and Boundary Conditions

As shown in Figure 3, the cross-sectional dimensions of the computational domain used in the numerical simulation were identical to those of the wind tunnel test section.

10.1029/2025JD045114

The boundary conditions of the computational domain were consistent with those of the wind tunnel. To prevent numerical errors arising from proximity between the outlet boundary and the obstacle, the computational domain was extended by 1.5 m in the streamwise direction. To more accurately capture the particle dynamics near the obstacle surface, local mesh refinement was applied in the central region and around the obstacle. The final mesh contained approximately 6 million cells, with a minimum grid spacing of 0.5 mm. The inlet velocity profile was specified based on the experimentally measured wind speed distribution and defined as $U = u^* \ln(z/z_0)/\kappa$, where $\kappa = 0.41$ is the von Kármán constant, u^* is the friction velocity, and z_0 is the surface roughness length. A 1 m-long precursor (recycling) domain was placed upstream of the main computational region to emulate an infinitely long domain. The flow was continuously recycled within this precursor zone until a fully developed turbulent boundary layer formed, which was then mapped onto the downstream domain. The top boundary of the computational domain was treated as a slip wall, the bottom boundary was set as a no-slip wall, enforcing $u|_{Z=0} = v|_{Z=0} = 0$. A wall function was applied to model near-wall flow characteristics. The surface roughness was set to $z_0 = 0.00003$ m, based on the sandpaper grit used in the wind tunnel experiments. Periodic boundary conditions were imposed in the spanwise direction. To avoid interference from particles within the precursor domain, particles were released 1.01 m downstream from the domain inlet at the centerline height. The release rate was set to $N = 10^5$ particles per second. The particle size distribution was assigned based on measurements from the aerosol spectrometer. The cylindrical obstacle was positioned along the centerline of the wind tunnel, located 2.8 m from the domain inlet. When particles impacted the top or bottom boundaries of the domain, they were considered deposited due to the adhesive nature of glycerol and were not allowed to continue moving. At the fluid outlet, a pressure outlet (zero-gradient) boundary condition was applied, and particles exiting the domain were treated as escaping freely. At each time step, the distance between each particle and the obstacle was calculated. A particle was considered deposited when the distance from its center to the obstacle surface was less than its radius. The physical properties of deposited particles were recorded, and their velocities were set to zero. The simulations were performed 30 s under a particle-free condition to allow the flow field to develop fully. Particle release was then initiated and continued for 120 s, after which deposition results were statistically analyzed. Consistent with the wind tunnel experiments, four simulation cases were conducted under different wind speeds.

4. Results and Discussion

4.1. Comparison of Experimental and Numerical Simulation Results

The mass of particles deposited on the obstacle surface was extracted from both the experimental measurements and the numerical simulations. Based on Equation 1, the collection efficiency was calculated separately for the experimental and numerical cases. The results are presented in Figure 4, which shows that the numerical simulation exhibited the same trend as the experimental data. To quantify the degree of dispersion between the experimental and numerical results, the correlation coefficient R_1 and the root-mean-square error R_2 were computed using the following formula:

$$R_1 = \frac{\sum\left(D_{\text{exp}} - \overline{D_{\text{exp}}}\right)\left(D_{\text{sim}} - \overline{D_{\text{sim}}}\right)}{\sqrt{\sum\left(D_{\text{exp}} - \overline{D_{\text{exp}}}\right)^2 \sum\left(D_{\text{sim}} - \overline{D_{\text{sim}}}\right)^2}},$$
$$R_2 = \sqrt{\frac{1}{n}\sum\left(D_{\text{sim}} - D_{\text{exp}}\right)^2} \tag{8}$$

in this equation, D_{exp} and D_{sim} represent the experimental and simulated deposition data, respectively. The resulting correlation coefficient was $R_1 = 0.9433$, and the root-mean-square error was $R_2 = 0.00664$. This high level of agreement confirms that the improved two-phase numerical simulation framework is capable of accurately reproducing the transport and deposition behavior of fine particles around obstacles.

4.2. Factors Affecting Particle Capture Processes by Surface Obstacles

To minimize the influence of the ground surface on the flow field and particle motion around the obstacle, our previous studies positioned the obstacle at the centerline height of the wind tunnel. However, the present study focused on simulating the dry deposition of atmospheric particles onto ground-mounted obstacles. After

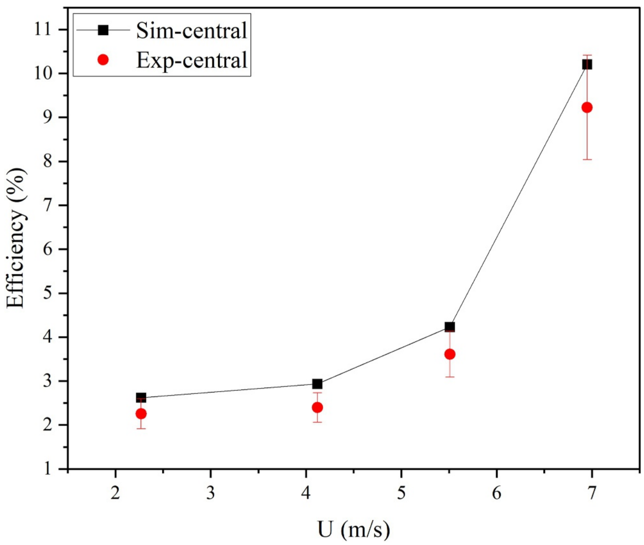

Figure 4. Comparison of collection efficiencies obtained from experimental and numerical simulations at different wind speeds. (The cylinder is positioned along the central axis; Error bars for experimental data represent the standard deviation from three replicate experiments).

confirming that the numerical simulation could reliably reproduce the experimental results, the obstacle was subsequently positioned on the ground surface for the following simulations. To better represent actual field conditions, the upper boundary of the computational domain was changed from a solid wall (as used in the validation cases) to a free-slip boundary. To improve computational accuracy, the vertical extent of the domain was doubled, resulting in overall domain dimensions of 3.5 × 0.6 × 0.3 m. This study primarily focuses on PM10 (i.e., particulate matter with an aerodynamic diameter less than or equal to 10 μm), so the particle size distribution was adjusted to follow a normal distribution ranging from 0.1 to 10 μm. The particle density was set based on the properties of dust aerosols. According to the characteristics of typical sandy surfaces (Wang & Zhao, 2005), the surface roughness length was specified as $z_0 = 0.00007$ m. Other initial and boundary conditions, obstacle dimensions, and mesh refinement strategies remained the same as those used in the previous simulation cases.

To visualize the flow field around the obstacle and facilitate the description of spatial deposition distributions, angular positions were defined along the obstacle surface, with the windward centerline assigned as 0° and the leeward centerline as ±180° (the inset diagram of Figure 5a).

We simulated particle capture on the obstacle surface under four wind speeds: 2.27, 4.12, 5.51, and 6.95 m/s. As Figure 5 shows, the total particle mass deposited on the obstacle surface over the simulation period was recorded. To analyze the spatial distribution of deposition, the cylindrical surface was geometrically unfolded into a rectangle, and the deposition mass was integrated along the vertical direction. The angular reference used for the unfolded surface corresponds to the angle definitions shown in the inset diagram of Figure 5a. After being released from the inlet, particles followed the flow field toward the obstacle. As the airflow diverted around the obstacle, particles with higher inertia impacted the windward side directly. Thus, inertial impaction was identified as the dominant deposition mechanism on the front surface of the obstacle. Some more flow-following particles, while not directly impacting the center of the windward face, were deposited in off-center windward zones due to interception. Here, particles moving close to the obstacle surface came into contact and stopped. The remaining particles continued along the flow path to the leeward side, where turbulence-induced deposition became significant, especially for particles with high followability that were entrained by wake vortices. Across the four wind speeds, the proportion of deposition on the windward side (−90° to 90°) accounted for 90.7%, 89.3%, 81.5% and 61.6% of the total deposition, respectively. These results indicate that as wind speed increased, particle deposition on the leeward side became more prominent due to enhanced turbulence-induced collisions. Two distinct deposition zones

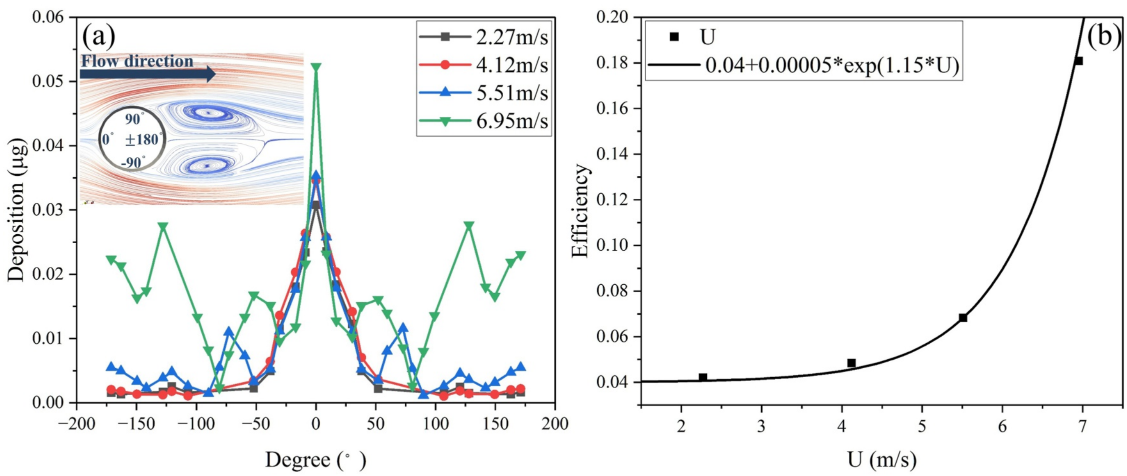

Figure 5. Particle deposition distribution (a) and collection efficiency (b) at different wind speeds (based on all particles deposited during a 120 s release period).

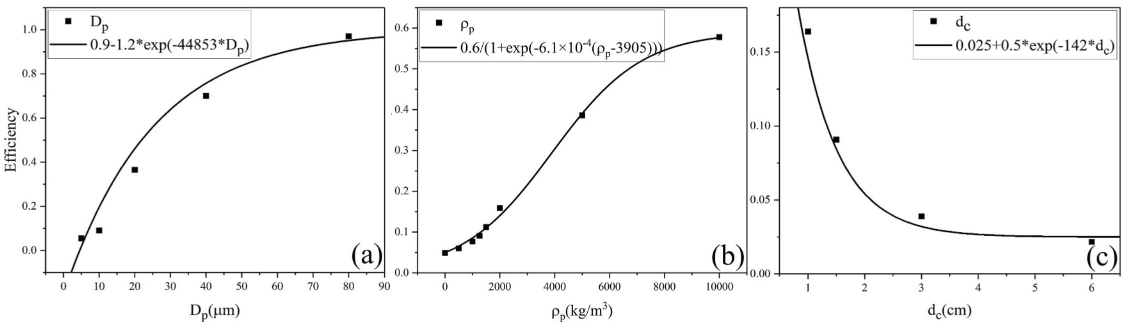

Figure 6. Influence of particle diameter (D_p), particle density (ρ_p) and roughness element size (d_c) on collection efficiency.

emerged on the windward face at 5.51 m/s within the angle ranges of −80° to −30° and 30° to 80°. Interception was the primary governing factor in these zones. When the wind speed increased to 6.95 m/s, the particle velocity increased further, and the locations of interception-induced deposition moved closer to the 0° region on the windward side. The share of particles deposited by interception in this region rose to 12% at 5.51 m/s and 15% at 6.95 m/s. In addition, higher wind speeds intensified turbulent fluctuations, causing the collection efficiency of particles on the surface of obstacles to increase exponentially.

To further investigate the influence of particle properties—specifically particle diameter (D_p) and density (ρ_p)—as well as obstacle size (d_c) on the deposition process, a series of simulations were conducted. The resulting collection efficiencies for each condition are presented in Figure 6.

As shown in Figure 6a, the particle collection efficiency increased rapidly with particle diameter (D_p). After this, the growth rate decreases gradually before finally reaching 100%. The focus of this paper is tiny particles, for larger particles, the collection efficiency will reach 100% in the ideal state. This means that particles with the same cross-section as the vertical direction of the obstacle will be completely deposited on the surface of the obstacle when they flow through it. With respect to particle density (ρ_p), Figure 6b shows that within the range considered in this study ($1\ \mathrm{kg/m^3} \le \rho_p \le 10{,}000\ \mathrm{kg/m^3}$), the collection efficiency increased rapidly at first and then gradually leveled off. It is important to note that real dust aerosol compositions rarely include substances with densities as high as $5000\ \mathrm{kg/m^3}$. It is clear that even in dust source regions, high-density particles will only be released under extreme wind conditions. These particles are also unlikely to be transported to high altitudes or over long distances. Therefore, the simulation cases using particle densities of $5000\ \mathrm{kg/m^3}$ and $10{,}000\ \mathrm{kg/m^3}$ were included to improve the curve fitting accuracy beyond the low-density regime. Fitting based solely on low-density particles is not adequate because it does not capture the nonlinear relationship between density and collection efficiency. Finally, as illustrated in Figure 6c, when the diameter of the cylindrical obstacle increased from 1 to 6 cm, the collection efficiency on its surface decreased sharply and then approached a plateau. Obstacle size primarily affects deposition caused by interception, which contributes far less to total deposition compared to inertial impaction. Therefore, changes in obstacle size had only a limited effect on collection efficiency per unit surface area.

Based on the different particle properties and obstacle sizes, the relationship between each parameter and the efficiency of particle deposition was derived as shown below:

$$\begin{aligned} E(D_p) &= B_1 + B_2 e^{B_3 * D_p}, \\ E(\rho_p) &= \frac{C_1}{1 + e^{C_2(\rho_p + C_3)}}, \\ E(d_c) &= D_1 + D_2 e^{D_3 * d_c}, \end{aligned} \tag{9}$$

the fitted parameters used in the collection efficiency functions were: $B_1 = 1.2$, $B_2 = -1.4$, $B_3 = -26{,}454$, $C_1 = 0.6$, $C_2 = -6.11 \times 10^{-4}$, $C_3 = -3905$, $D_1 = 0.025$, $D_2 = 0.5$, and $D_3 = -142$.

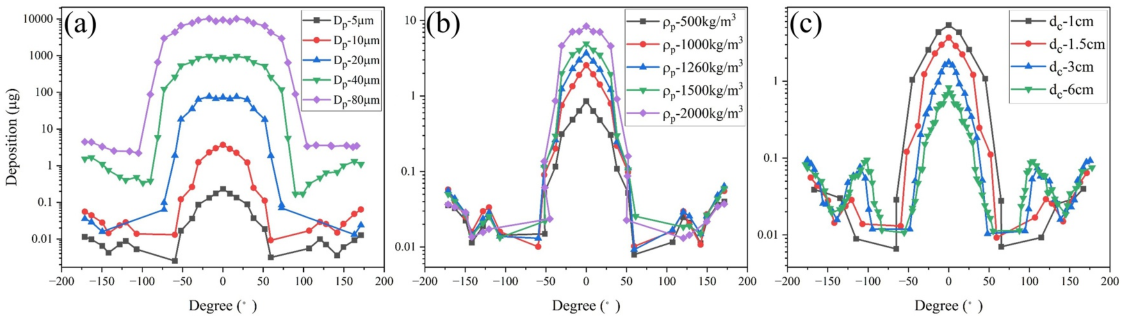

Figure 7. Influence of particle diameter (D_p), particle density (ρ_p) and obstacle size (d_c) on collection efficiency.

After establishing the relationships between particle collection efficiency and key influencing parameters, the particle deposition mass on the obstacle surface was extracted and analyzed. The influence of each parameter on both the spatial distribution of deposited particles and the governing deposition mechanisms is further discussed, as illustrated in Figure 7.

As shown in Figure 7a, when particle diameter increased, the mass of individual particles also increased, leading to greater deposition on the windward side of the obstacle. Furthermore, particles with diameters exceeding 10 μm were less influenced by turbulent fluctuations. As a result, under small-particle conditions ($D_p \leq 10$ μm), leeward-side deposition—primarily caused by turbulence-induced collisions—gradually diminished as particle diameter increased. This study's emphasis on fine particles, whose motion is more sensitive to flow structures, is therefore well-founded. Meanwhile, as the particle diameter increased, the windward deposition zone expanded. This was because more particles were deposited through interception rather than direct inertial impaction. A similar pattern was observed for particle density, as shown in Figure 7b. As particle density increased, the vortex-induced leeward deposition region also diminished. However, unlike particle size, increasing density enhanced inertial impaction but had little influence on interception. As a result, the spatial distribution of deposition on the windward side remained largely consistent across different densities. Although higher density increased the total deposited mass, the effect was less pronounced than that of particle diameter, since mass scales linearly with density. Additionally, higher-density particles were less likely to be entrained by shed vortices, leading to a further reduction in leeward deposition. Finally, the influence of obstacle size on deposition distribution is illustrated in Figure 7c. Increasing the obstacle diameter caused little change in the overall deposition distribution. Although larger obstacles correspond to higher Reynolds numbers, the range (10^3 to 10^5) remained within the regime where the flow structure around a cylindrical obstacle is qualitatively similar (Acheson, 1991). Apparent changes in the deposition distribution were largely due to geometric differences in arc curvature: for a given arc length, smaller-diameter cylinders subtended larger central angles.

4.3. Relationship Between Stokes Number and Collection Efficiency

Based on the above results, the particle collection efficiency on the obstacle surface was found to be significantly influenced by the inflow velocity, particle diameter, particle density, and obstacle size. The parameters under consideration are all found to be related to the Stokes number (Stk), which is a key dimensionless parameter that characterizes the inertial behavior of particles relative to the surrounding fluid. According to the definition proposed by Fuchs et al. (1965), the Stokes number is given by:

$$St = \frac{\tau_p u}{d_c}, \tag{10}$$

here, u refers to the fluid velocity as it passes around the obstacle, d_c denotes the characteristic length scale of the obstacle, and the particle relaxation time is given by $\tau_p = \frac{C_c \rho_p D_p^2}{18\mu}$. To account for the influence of turbulence on particle deposition, Moran et al. (2013) proposed a modified form known as the turbulent Stokes number:

$$St^* = St \cdot Re_\lambda^{0.3}, \tag{11}$$

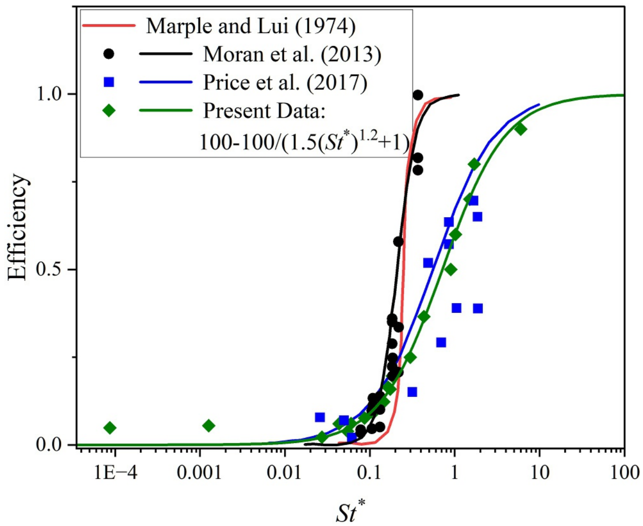

Figure 8. Influence of the turbulence Stokes number on collection efficiency. Points represent experimental and simulated data; lines represent fitted curves.

the classical Stokes number was further refined by incorporating the Taylor microscale Reynolds number, defined as $Re_\lambda = \sigma_u \lambda / \nu$, where σ_u is the local root-mean-square (r.m.s.) velocity fluctuation, λ is the turbulence length scale representing the smallest eddies in the region, and ν is the kinematic viscosity of the fluid. By substituting the wind field characteristics, particle properties, and obstacle dimensions into Equation 11, the relationship between the turbulent Stokes number and collection efficiency was established. The results are shown in Figure 8. The black dots and line represent the simulation results from this study. For comparison, the red line shows the theoretical collection efficiency under laminar conditions proposed by Marple and Liu (1974). The blue line represents the wind tunnel results obtained by Moran et al. (2013) for particle deposition on flat plate surfaces. The green line corresponds to the modified empirical fit proposed by Price et al. (2017), which corrected the effective collection area to account for non-impaction deposition and used real vegetation in the experiments. Our simulation results aligned closely with the experimental results of Price et al. (2017), exhibiting excellent agreement and high fitting accuracy. The specific fitted functions and statistical goodness-of-fit metrics for all models are listed in Table 1.

As shown in Figure 8, when the turbulent Stokes number was below 0.01 ($St^* \leq 0.01$), viscous drag dominated the particle dynamics. Under these conditions, particles exhibited high followability with the flow, and deposition on the obstacle surface was primarily governed by turbulence-induced mechanisms. As a result, the overall collection efficiency remained below 4%. As St^* increased within the range $0.01 < St^* \leq 1$, inertial impaction and interception began to contribute significantly to the deposition process. In this transition regime, the collection efficiency rose sharply—by more than 70%—indicating a shift from turbulence-dominated to inertia-enhanced particle behavior. When the turbulent Stokes number exceeded 1 ($St^* > 1$), deposition was almost entirely driven by inertial impaction. Particles with sufficient inertia impacted the windward surface of the obstacle directly. Assuming negligible rebound and other loss mechanisms, the collection efficiency approached 100% asymptotically in this regime.

5. Conclusion

This study investigated the particle deposition process on the surface of an isolated cylindrical obstacle through a combined approach involving wind tunnel experiments and numerical simulations. The effects of particle properties and obstacle size on deposition were analyzed, and a fitted curve describing the relationship between collection efficiency and turbulent Stokes number was developed. The main conclusions are as follows:

1. The deposition of particles was predominantly observed on the windward side of the obstacle, where the predominant mechanisms were inertial impaction and interception. As the inflow velocity increased, the deposition of particles on the leeward side—driven by turbulence-induced impaction—became progressively more significant.
2. It is evident that both the properties of particles and the dimensions of obstacles exert a significant influence on the process of deposition. Specifically, larger particle diameters enhanced deposition via interception, while increasing particle density promoted deposition through inertial impaction. However, changes in obstacle size had a relatively minor influence on deposition characteristics and spatial distribution.
3. The relationship between particle collection efficiency and the turbulent Stokes number was captured by the following fitted equation: $DF = 100 - 100/\left(1.5(St^*)^{1.2} + 1\right)$, Compared to existing experimental results, this fitted model demonstrated superior accuracy and consistency.

This work focuses on particle deposition onto isolated obstacles near the surface, providing mechanistic insights into the near-ground deposition process. Clarifying particle–obstacle interaction mechanisms under simplified configurations lays the groundwork for future studies involving complex, multi-obstacle terrains. Understanding these dynamics is a prerequisite for

Table 1
Model Fit Comparison Between Marple and Liu (1974) Laminar Data, Moran et al. (2013) Idealized Substrates, Price et al. (2017) Artificial Vegetation, and the Present Work

Fit	Equation	r^2
Marple and Liu (1974)	–	0.15
Moran et al. (2013)	$E = 100 - \frac{100}{400.5(St^*)^{3.88} + 1}$	0.42
Price et al. (2017)	$E = 100 - \frac{100}{2.049(St^*)^{1.19} + 1}$	0.65
Present Work	$E = 100 - \frac{100}{1.5(St^*)^{1.2} + 1}$	0.99

improving near-surface particle concentration modeling and refining dry deposition parameterizations in atmospheric aerosol models. Ongoing research is extending this framework to more realistic surface conditions with multiple interacting obstacles.

Conflict of Interest

The authors declare no conflicts of interest relevant to this study.

Data Availability Statement

Data of the present work is available from Gong et al. (2025) via: https://doi.org/10.5281/zenodo.16777960.

Acknowledgments

This research has been supported by the National Natural Science Foundation of China (42376232), the National Key Research and Development Program of China (2023YFF130420304), the Key Technology Research Project of TW-3 (TW3006) and Supercomputing Center of Lanzhou University. Numerical simulations presented in this study are carried out with customized versions of the OpenFOAM toolkit.

References

Acheson, D. J. (1991). *Elementary fluid dynamics*. Acoustical Society of America.

Bache, D. (1979). Particle transport within plant canopies—I. A framework for analysis. *Atmospheric Environment*, *13*(9), 1257–1262. https://doi.org/10.1016/0004-6981(79)90080-5

Chamberlain, A. (1968). Transport of gases to and from surfaces with bluff and wave-like roughness elements. *Quarterly Journal of the Royal Meteorological Society*, *94*(401), 318–332. https://doi.org/10.1002/qj.49709440108

Chapman, S., & Cowling, T. G. (1990). *The mathematical theory of non-uniform gases: An account of the kinetic theory of viscosity, thermal conduction and diffusion in gases*. Cambridge University Press.

Clift, R., Grace, J. R., & Weber, M. E. (1978). *Bubbles, drops, and particles*. Academic Press.

Droppo, J. G. (2006). *Improved formulations for air-surface exchanges related to national security needs: Dry deposition models*. Pacific Northwest National Lab (PNNL). https://doi.org/10.2172/890729

Fuchs, N. A., Daisley, R., Fuchs, M., Davies, C., & Straumanis, M. E. (1965). *The mechanics of aerosols*. American Institute of Physics. https://doi.org/10.1063/1.3047354

Gong, K., Zhang, J., Chen, Q., Xi, X., Cheng, X., Huang, N., & Huang, Z. (2025). Mechanisms controlling dust aerosol collection by isolated obstacles near the ground. https://doi.org/10.5281/zenodo.16777960

Gong, K., Zhang, J., Huang, N., Shao, Y., & Li, X. (2024). A numerical study on the collection efficiency of devices for atmospheric dust deposition. *Catena*, *236*, 107736. https://doi.org/10.1016/j.catena.2023.107736

Gritskevich, M. S., Garbaruk, A. V., Schütze, J., & Menter, F. R. (2012). Development of DDES and IDDES formulations for the k-omega shear stress transport model. *Flow, Turbulence and Combustion*, *88*(3), 431–449. https://doi.org/10.1007/s10494-011-9378-4

Gu, Z. (2007). *Eolian dust*. Science Press.

Li, A., & Ahmadi, G. (1992). Dispersion and deposition of spherical particles from point sources in a turbulent channel flow. *Aerosol Science and Technology*, *16*(4), 209–226. https://doi.org/10.1080/02786829208959550

Ma, G., & Zheng, X. (2011). The fluctuation property of blown sand particles and the wind-sand flow evolution studied by numerical method. *The European Physical Journal E*, *34*(5), 1–11. https://doi.org/10.1140/epje/i2011-11054-3

Mahowald, N. M., Baker, A. R., Bergametti, G., Brooks, N., Duce, R. A., Jickells, T. D., et al. (2005). Atmospheric global dust cycle and iron inputs to the ocean. *Global Biogeochemical Cycles*, *19*(4). https://doi.org/10.1029/2004gb002402

Malet, J., Alloul, L., Michielsen, N., Boulaud, D., & Renoux, A. (2000). Deposition of nanosized particles in cylindrical tubes under laminar and turbulent flow conditions. *Journal of Aerosol Science*, *31*(3), 335–348. https://doi.org/10.1016/S0021-8502(99)00062-2

Marple, V. A., & Liu, B. Y. (1974). Characteristics of laminar jet impactors. *Environmental Science & Technology*, *8*(7), 648–654. https://doi.org/10.1021/es60092a003

Martinelli, N., Olivieri, O., & Girelli, D. (2013). Air particulate matter and cardiovascular disease: A narrative review. *European Journal of Internal Medicine*, *24*(4), 295–302. https://doi.org/10.1016/j.ejim.2013.04.001

Menter, F. R. (1994). Two-equation eddy-viscosity turbulence models for engineering applications. *AIAA Journal*, *32*(8), 1598–1605. https://doi.org/10.2514/3.12149

Moran, S. M., Pardyjak, E. R., & Veranth, J. M. (2013). Understanding the role of grid turbulence in enhancing PM10 deposition: Scaling the stokes number with Rλ. *Physics of Fluids*, *25*(11), 115103. https://doi.org/10.1063/1.4829451

Pan, Y., & Wang, Y. (2015). Atmospheric wet and dry deposition of trace elements at 10 sites in northern China. *Atmospheric Chemistry and Physics*, *15*(2), 951–972. https://doi.org/10.5194/acpd-14-20647-2014

Petroff, A., Mailliat, A., Amielh, M., & Anselmet, F. (2008a). Aerosol dry deposition on vegetative canopies. Part I: Review of present knowledge. *Atmospheric Environment*, *42*(16), 3625–3653. https://doi.org/10.1016/j.atmosenv.2007.09.043

Petroff, A., Mailliat, A., Amielh, M., & Anselmet, F. (2008b). Aerosol dry deposition on vegetative canopies. Part II: A new modelling approach and applications. *Atmospheric Environment*, *42*(16), 3654–3683. https://doi.org/10.1016/j.atmosenv.2007.12.060

Price, T. A., Stoll, R., Veranth, J. M., & Pardyjak, E. R. (2017). A wind-tunnel study of the effect of turbulence on PM10 deposition onto vegetation. *Atmospheric Environment*, *159*, 117–125. https://doi.org/10.1016/j.atmosenv.2017.03.043

Pye, K. (2015). *Aeolian dust and dust deposits*. Elsevier.

Saini, R., Karimi, N., Duan, L., Sadiki, A., & Mehdizadeh, A. (2018). Effects of near wall modeling in the improved-delayed-detached-eddy-simulation (IDDES) methodology. *Entropy*, *20*(10), 771. https://doi.org/10.3390/e20100771

Shao, Y. (2008). *Physics and modelling of wind erosion*. Springer.

Shao, Y., Wyrwoll, K.-H., Chappell, A., Huang, J., Lin, Z., McTainsh, G. H., et al. (2011). Dust cycle: An emerging core theme in earth system science. *Aeolian Research*, *2*(4), 181–204. https://doi.org/10.1016/j.aeolia.2011.02.001

Smoke, S. (1977). *Dust and haze: Fundamentals of aerosol behavior*. John Wiley & Sons. https://doi.org/10.1029/JB085iB12p07247

Tong, D., & Huang, N. (2012). Numerical simulation of saltating particles in atmospheric boundary layer over flat bed and sand ripples. *Journal of Geophysical Research*, *117*(D16). https://doi.org/10.1029/2011JD017424

Wang, T., & Zhao, H. (2005). Fifty-year history of China desert science. *Journal of Desert Research*, *25*(2), 145–165. https://doi.org/10.1360/biodiv.050058

Xu, B., Zhang, J., Huang, N., Gong, K., & Liu, Y. (2018). Characteristics of turbulent aeolian sand movement over straw checkerboard barriers and formation mechanisms of their internal erosion form. *Journal of Geophysical Research: Atmospheres*, *123*(13), 6907–6919. https://doi.org/10.1029/2017JD027786

Zhang, J., & Shao, Y. (2014). A new parameterization of particle dry deposition over rough surfaces. *Atmospheric Chemistry and Physics*, *14*(22), 12429–12440. https://doi.org/10.5194/acp-14-12429-2014